Published in final edited form as:
Nat Methods. 2019 June ; 16(6): 545–552. doi:10.1038/s41592-019-0398-7.

Light Sheet Microscopy in the Near-Infrared II Window

Feifei Wang[1,†], **Hao Wan**[1,†], **Zhuoran Ma**[1,†], **Yeteng Zhong**[1], **Qinchao Sun**[1], **Ye Tian**[1], **Liangqiong Qu**[2], **Haotian Du**[1], **Mingxi Zhang**[3], **Lulin Li**[4], **Huilong Ma**[5], **Jian Luo**[4,6], **Yongye Liang**[5], **Wen Jung Li**[7,8], **Guosong Hong**[9], **Lianqing Liu**[7], and **Hongjie Dai**[1,*]

[1]Department of Chemistry and Bio-X, Stanford University, Stanford, California, USA.

[2]Department of Radiology and BRIC, University of North Carolina at Chapel Hill, Chapel Hill, North Carolina, USA.

[3]State Key Laboratory of Advanced Technology for Materials Synthesis and Processing, Wuhan University of Technology, Wuhan, China

[4]Palo Alto Veterans Institute for Research, VA Palo Alto Health Care System, Palo Alto, California, USA.

[5]Department of Materials Science and Engineering, South University of Science and Technology of China, Shenzhen, China.

[6]Department of Neurology and Neurological Sciences, Stanford University School of Medicine, Stanford, California, USA.

[7]State Key Laboratory of Robotics, Shenyang Institute of Automation, Chinese Academy of Sciences, Shenyang, China.

[8]Department of Mechanical and Biomedical Engineering, City University of Hong Kong, Kowloon Tong, Hong Kong.

[9]Department of Materials Science and Engineering, Stanford University, Stanford, California, USA.

Abstract

Deep-tissue three-dimensional (3D) optical imaging of live mammals with high spatiotemporal resolution in non-invasive manners has been challenging due to light scattering. Here, we developed near-infrared II (NIR-II, 1000–1700 nm) light sheet microscopy (LSM) with excitation and emission up to ~ 1320 nm and ~ 1700 nm respectively for optical sectioning through live

---

[*] Correspondence should be addressed to: hdai@stanford.edu.

Author contributions

Hongjie D. and F.W. conceived and designed the experiments. Hongjie D. and F.W. designed the optical system. F.W. set up the optical system. F.W., H.W., Z.M. and Y.Z. performed the experiments. Q.S. did the Monte Carlo simulations. F.W., H.W., Z.M., Y.Z., Q.S., Y.T., L.Q., Haotian D., H.M., Y.L., W.J.L., G.H., L.L. and Hongjie D. analyzed the data. M.Z. developed the PbS/CdS CSQD dyes. F.W., W.H., Z.M., and Hongjie D. wrote the manuscript. L.L and J.L. performed TBI. All authors contributed to the general discussion and revision of the manuscript.

[†] These authors contribute equally to this work.

Competing Financial Interests Statement

Authors declare no competing interests.

tissues at ~ 750-μm penetration depth without any invasive surgery. Suppressed light scattering allowed imaging at ~ 2 mm depth in glycerol-cleared brain tissues. NIR-II LSM in normal and oblique configurations enabled *in vivo* imaging of live mice through intact tissue, revealing abnormal blood flow and T cell motion in tumor microcirculation and mapping out programmed-death ligand 1 (PD-L1) and programmed cell death protein 1 (PD-1) in tumors with cellular resolution. 3D imaging through intact mouse head resolved vascular channels between skull and brain cortex, and monitored recruitment of macrophages/microglia to traumatic brain injury site post injury.

Introduction

Optical imaging of biological systems capable of high spatiotemporal resolution *in vivo* and *ex vivo* has revolutionized biology and medicine for visualization and understanding of structures, functions and dynamic processes at the cellular and even molecular scale[1,2]. To circumvent light scattering by tissues, *in vivo* 3D imaging by nonlinear two-photon fluorescence microscopy (670–1070 nm excitation)[3–5] or three-photon microscopy (1300–1700 nm excitation)[6–9] has reached penetration depths ~ 0.7–1.5 mm, benefiting from increased scattering mean free path of the near-infrared (NIR) excitation employed[6]. Light sheet microscopy (LSM) uses orthogonally arranged planar illumination and wide-field detection, capable of high speed 3D optical sectioning, low photo-damage[10,11] and volumetrically imaging/tracking with subcellular resolution[2]. Currently the excitation and emission of LSM are mostly in the visible except for two photon excitation in the NIR at ~ 940 nm[12] or three photon excitation at 1000 nm[13]. Light scattering has limited LSM to imaging small transparent animals, organisms (zebrafish larvae, drosophila larvae, Medaka embryo, *C. elegans, etc.*), mammalian tissue samples after chemical clearing[11,14,15], and mouse brain at a depth of ~ 200 μm after craniotomy[16].

In recent years several classes of fluorescence probes have been developed with emission in the NIR-II window (1000–1700 nm) including carbon nanotubes, quantum dots, organic conjugated polymers and molecular dyes, and rare-earth nanoparticles[17–30]. With suppressed photon scattering and diminished autofluorescence in the long-wavelength region, these probes have facilitated one-photon wide-field[17–27] or confocal[28,29] fluorescence imaging in the NIR-II window for mouse models of cardiovascular and brain diseases and cancer[20,28,30]. Non-invasive imaging through the skin, skull and body tissues was achieved, with deep penetration depths and high signal-to-background ratio (SBR). Here, we developed NIR-II LSM using organic dyes and PbS/CdS core/shell quantum dot (CSQD) probes, extending excitation and emission to the unprecedented ~ 785–1320 nm and ~ 1000–1700 nm regimes respectively. Suppressed light scattering of both excitation and emission allowed up to 10 mm^3 volumetric imaging of glycerol-cleared mouse brain *ex vivo* with a penetration depth of ~ 2 mm. Importantly, NIR-II LSM readily afforded *in vivo* imaging of mouse tumor and traumatic brain injury (TBI) models non-invasively, enabling real-time observation of unusual tumor microcirculation, 3D tracking recruitment of macrophages/microglia to injury region and 3D molecular imaging of immune checkpoint proteins at cellular scale in live mammals.

Results

Light scattering suppression in NIR-II LSM.

Our home-built LSM employed multiple switchable lasers with Gaussian beams (658 nm, 785 nm and 1319 nm) cylindrically focused into static light sheets for optical sectioning and an InGaAs camera for orthogonally detecting 900–1700 nm fluorescence (Fig. 1a and see setup details in Supplementary Fig. 1). We adjusted the effective numerical apertures of illumination objectives to produce light sheets with balanced waist thickness (~ 10–20 μm) and Rayleigh length (~ 0.5–2.0 mm) (see Methods for light sheet shape analysis), suitable for large scale volumetric imaging with single cell resolution. We employed several biocompatible NIR-II probes, an organic nanofluorophore p-FE[28] (excitation/emission: 650–850 nm/1000–1300 nm, Fig. 1b and Supplementary Fig. 2, dynamic light scattering size ~ 12 nm) and PEGylated PbS/CdS CSQD probes[29] (excitation/emission: ultraviolet to 1500 nm/1500–1700 nm, Fig. 1b and Supplementary Fig. 2, size ~ 6.9 nm). The two probes were sequentially injected intravenously into a mouse through the tail-vein at an interval of 5 min. We sacrificed the mouse at 30 min post injection while the probes were still circulating in the vasculature, fixed the brain and placed it in glycerol for *ex vivo* LSM imaging (see Methods for details). Under the same 785 nm light sheet (LS) excitation, we were able to clearly image the cerebral vasculatures as a function of tissue depth Z in three fluorescence emission windows 850–1000 nm (NIR-I, p-FE emission), 1100–1200 nm (NIR-IIa, p-FE emission) and 1500–1700 nm (NIR-IIb, CSQD emission) respectively (Fig. 1c and Supplementary Video 1). This allowed side-by-side comparison (Fig. 1c and Supplementary Fig. 3) of fluorescence LSM imaging in three sub-regions of 850–1700 nm under the same 785 nm LS excitation. Note that refractive index mismatch during scanning was compensated by linearly moving detection objective (Supplementary Figs 4 and 5) and no photobleaching was observed through this work, owing to the highly photo-stable NIR-II probes and minimal photo damage inherent to LSM[10,11].

With a 785 nm light sheet, we observed that the glycerol-cleared brain tissue imaging depth limit increased (Fig. 1c and Supplementary Video 1), background signal decreased (Fig. 1d) and SBR increased (Fig. 1e) at longer detection wavelength from 850–1000 nm to 1100–1200 nm and 1500–1700 nm (Supplementary Video 1). The imaging depth limit (defined as tissue depth at which SBR decreased to ~ 2) increased from $Z_{\mathrm{SBR}=2}$ ~ 1.0 mm to ~ 2.0 mm and ~ 2.5 mm as emission wavelength increased from ~ 850 nm to ~ 1100 nm and ~ 1700 nm (Fig. 1e and Supplementary Video 1). These were direct results of suppressed scattering of emission photons (scattering $\propto \lambda^{-k}$, where λ is wavelength and k is in the range of 0.2–4.0 for biological tissues[20]) under the same 785 nm excitation. Background signal caused by scattering was the lowest in the 1500–1700 nm emission range at all imaging depths (Z up to 3 mm, Fig. 1d and Supplementary Video 1). For emission in the 850–1200 nm range, background signal increased with tissue imaging depth up to $Z = \sim 1$ mm due to increased scattering by thicker tissue and decreased upon further increases in depth for $Z > 1$ mm (Fig. 1d). The latter was attributed to increased light absorption by thicker tissue that attenuated the background signal.

The lateral full width at half maximum (FWHM) values of the smallest cerebral vasculatures imaged in the three emission regions (850–1000 nm, 1100–1200 nm and 1500–1700 nm, Fig. 1f) at their tissue imaging depth limits of $Z_{\mathrm{SBR}=2}$ = 1.0 mm, 2.0 mm and 2.5 mm were ~ 7.2 μm, 9.0 μm and 8.3 μm respectively. Using an imaging objective with high magnification and numerical aperture (NA), < 5.0 μm lateral FWHM was achieved by NIR-II LSM imaging by detecting 1500–1700 nm emission under a 785 nm LS illumination (Supplementary Fig. 6).

As a light sheet propagated in a scattering medium such as an intralipid phantom[31,32] mimicking the glycerol-cleared brain tissue, Monte Carlo simulations[33] and experiments observed light sheet decaying in intensity in the X-Y plane and spreading in Z due to tissue scattering (Fig. 2a–d, Supplementary Figs 7–10), which could hinder optical sectioning capability with reduced imaging field of view in X-Y and lower spatial resolution in Z. To circumvent this and maximize the benefit of reduced photon scattering at long wavelengths, we constructed a 1320 nm light sheet to afford the lowest degree of intensity decay and the least LS thickness broadening relative to the 785 nm and 658 nm light sheets (Fig. 2a–d, Supplementary Figs 8–10). In the glycerol-cleared brain tissue, 658 nm, 785 nm and 1319 nm light sheets propagated over a distance of ~ 1.3 mm, ~ 1.7 mm and ~ 4.0 mm respectively (Fig. 2a), within which imaging of cerebral vasculatures by detecting 1500–1700 nm fluorescence of PbS/CdS core-shell quantum dots could still resolve small vessels (FWHM < 10 μm).

It constituted a breakthrough for one-photon imaging exploiting long wavelength excitations up to 1319 nm (Supplementary Fig. 2). Excitingly, the 1319 nm light sheet could propagate > 6 mm to allow imaging of large blood vessels in the glycerol-cleared mouse brain over large field of views (Fig. 2a). Suppressed scattering of longer wavelength LS was also gleaned from X-Y, X-Z or Y-Z cross sectional images (Fig. 2e, Supplementary Fig. 11 and Supplementary Videos 2 and 3), with improved SBR (Fig. 2f) and reduced FWHM of feature sizes along the depth Z direction, corresponding to higher vertical resolution and better sectioning capability along Z (Supplementary Fig. 11).

Light sheet microscopy with both excitation and emission in the 1000–1700 nm NIR-II window minimized scattering and maximized the penetration depth and field of view. High resolution 3D NIR-II LSM sectioning (Supplementary Fig. 12a and Supplementary Video 4, volume = 810 μm × 648 μm × 3000 μm, 3 μm Z increment in depth, maximum Z ~ 2.5 mm) afforded sub-10 μm × 10 μm × 15 μm volumetric resolution (FWHM) in glycerol-cleared brain tissue (Fig. 1f and Supplementary Fig. 11).

Under the 785 nm LS excitation, the maximum 1500–1700 nm fluorescence signal detected in the cerebral vasculatures of glycerol-cleared mouse brain cortex layer as a function of depth Z showed two attenuation regions (Supplementary Fig. 12e). There was an initial exponential attenuation due to reduction in ballistic and nearly ballistic photons (slightly deflected) emerging through the tissue following the Beer–Lambert law $I_{\mathrm{ball}} = I_0\, e^{-z/l_s}$ (where z is imaging depth, I_0 is initial intensity at $Z = 0$ mm and l_s is scattering mean free path MFP). This was followed by a slower decay region at deeper Z from which multiply scattered photons diffusing through the brain tissue (diffusive region) were dominant[34]. The

MFP l_s extracted (Supplementary Fig. 12e) for glycerol-cleared brain tissue was ~ 305 μm, ~ 440 μm and ~ 639 μm in the 850–1000 nm, 1100–1200 nm and 1500–1700 nm windows respectively, about twice of that of non-cleared brain tissue[35]. The imaging penetration depth limits (see Supplementary Table 1 for detailed scattering coefficients and MFP comparison) were ~ $2.5l_s$ (for 850–1000 nm emission), ~ $2.6l_s$ (for 1100–1200 nm emission) and ~ $3.3l_s$ (for 1500–1700 nm emission).

Non-invasive *in vivo* optical sectioning of live mice by NIR-II LSM.

The capability of NIR-II LSM performing volumetric imaging through scattering tissues at the 1–10 mm^3 scale enabled non-invasive *in vivo* 3D imaging disease models of live mice (Fig. 3), facilitating cellular resolution LS sectioning through intact tissues for mammals. We carried out NIR-II LSM imaging of subcutaneous xenograft tumors on mice ear and right/left flank of back without invasive surgery or installing optical windows[36]. Non-invasive *in vivo* hemodynamic imaging of a tumor model used for immunotherapy, murine colorectal MC38 tumors on C57BL/6 mice ear was carried out with the NIR-II light sheet fixed at a Z position ~ 300 μm below the top (where the fluorescence signal was first detected) of the tumor (~ 8 mm in diameter, Fig. 3a,b). Time-course LS imaging of the p-FE nanofluorophore immediately following intravenous injection into the mouse tail-vein (785 nm excitation, 1000 nm detection at exposure times ~ 100–800 ms) revealed abnormal microcirculation in tumor. Blood flows in tumor vasculatures were found irregular and intermittent (Fig. 3a,c and Supplementary Video 5), with turning-on and shutting-off behavior, oscillatory/fluctuating flowing patterns and even flow direction reversal in the same vasculature (Fig. 3c, marked by arrows, Supplementary Video 5). These observations suggested unstable pressure within a tumor due to uncontrolled tumor angiogenesis. Further, blood supply time (BST, defined as the time at which the pixel intensity reached its maximum value relative to the fluorescence flow is first detected) analysis revealed that the p-FE nanofluorophore gradually leaked out from some vasculatures (in the red-colored region in Fig. 3d) but not from others (in the black-colored region in Fig. 3d). Detailed experimental conditions were summarized in Supplementary Table 2.

PD-L1 is an important immune checkpoint protein expressed by certain tumors as a powerful way of cancer evasion of a body’s immune surveillance through PD-L1 (on tumor) and PD-1 (on T cells) binding[37]. PD-L1 blocking by antibody immunotherapy is a breakthrough approach to activate the immune system and treat cancer. *In vivo* PD-L1 imaging/mapping is important to fundamental understanding of cancer immunity and immunotherapy mechanism[37,38]. To this end, we developed a 45° oblique NIR-II LSM (Fig. 3e and Supplementary Fig. 1b) and performed non-invasive *in vivo* three-plex molecular imaging of PD-L1 expressing CT26 tumor[39]. An erbium-based rare-earth nanoparticles (ErNPs)[25] (excitation 975 nm/emission 1500–1700 nm, see Method) conjugated to PD-L1 antibodies were injected intravenously and 24 h later, PEGylated PbS/CdS CSQD conjugated to anti-PD-1 (excitation ~ 1319 nm/emission 1500–1700 nm) were injected. At 2 h post injection, dynamic imaging into the tumor at a fixed illumination plane by oblique NIR-II LSM (Fig. 3e) observed a single PD-1+ T cell (labeled by PEGylated PbS/CdS CSQDs) circulating in tumor vasculatures irregularly and following blood flow direction reversal (Fig. 3f and Supplementary Video 6). In another 27 h, p-FE was injected intravenously for labeling tumor vessels. Wide-field imaging was first used to image PD-L1 and PD-1 labelled by anti-PD-L1-ErNPs and anti-PD-1-CSQD respectively (Fig. 3g), and fluorescence signals of ErNPs and PbS/CdS CSQD (both in 1500–1700 nm range) were differentiated by resolving the vastly different lifetimes of the two probes (~ 5 ms for ErNPs and ~ 20 μs for PbS, see Method). We then performed 3-plex oblique NIR-II LSM to profile the 3D spatial distribution of PD-L1, PD-1 and vasculatures (labeled by circulating p-FE in 1100–1300 nm channel) in tumor (Fig. 3h) through the intact skin on the tumor without installing invasive window chamber (Fig. 3i). We observed PD-1 expressing T cells extravasated out of vessels (Fig. 3h) and surrounding PD-L1 expressing cells in the tumor, an important step in initiating cancer cell killing immunotherapeutic effect (Fig. 3h,j and Supplementary Video 7). These results demonstrated multiplexed molecular imaging in 3D using oblique NIR-II LSM, which could be particularly useful for longitudinal imaging over long times due to its non-invasive nature. With this modality, sub-6-μm FWHM in the lateral X-Y plane and sub-15-μm FWHM in Z using a 50X detection objective can be realized (Supplementary Figs 13–14), useful for cellular scale molecular imaging of multiple targets *in vivo*.

Strong scattering of light by scalp/skull typically required scalp removal[40,41]. To demonstrate non-invasive oblique NIR-II LSM into non-protruding tissues, we imaged intact mouse head through the layers of scalp, skull, meninges and brain cortex, 2 h post injection of PEGylated PbS/CdS CSQD probes (Fig. 4a,b). The 1319-nm illumination and 1500–1700-nm fluorescence detection afforded a penetration depth of ~ 774 μm along the tilted light sheet direction into the head using a 10X imaging objective (Fig. 4c) with 7–15-μm FWHM in X-Y plane and 7–17-μm FWHM along Z direction, gleaned by measuring the smallest vessels (Supplementary Fig. 15). In the meninges, interesting vascular channel like structures connecting the skull bone and brain cortex (marked by triangles in Fig. 4a,d) were observed. These channels could be important to immune system of the brain revealed recently[42] and were resolved here for the first time by a non-invasive LSM imaging *in vivo*.

Further, in a mouse model of TBI[43] (Fig. 4e), the meningeal macrophages/microglia were labelled by intravenously injected anti-CD11b-PEGylated PbS/CdS CSQD 2 h after injury. At 24 h post injection, non-invasive 3D time-course LSM imaged/monitored the recruitment of meningeal macrophages/microglia to the injured site as an inflammatory response[44] (Fig. 4f and Supplementary Video 8).

Discussion

This work developed 3D near-infrared light sheet microscopy for *in vivo* and *ex vivo* deep tissue volumetric imaging through highly scattering biological tissues. Light sheet microscopy with both excitation and emission in the NIR-II window avoided shadows or stripes along the illumination direction by suppressing tissue scattering and adsorption effects encountered by visible LSM[45]. Non-invasive NIR-II LSM enabled *in vivo* observation in wide-field detection mode with suppressed background, facilitating dynamic process tracking and molecular imaging at cellular resolution over millimeter scale. NIR-II LSM provides a complementary method to two-photon microscopy at a lower cost and under less invasive conditions (Supplementary Table 3). NIR-II LSM imaging can be further advanced by developing brighter fluorophores, applying new configurations of LSM[46] and using InGaAs camera with lower readout noise and dark current[47]. Recent developments such as noncoherent structured illumination[48] and optical lattices illumination[2] could be introduced to improve the resolution and contrast of NIR-II LSM. Real time molecular imaging of multiple targets by rapid sectioning 3D tissues of live mammals should become possible.

Methods

NIR-II fluorescence probes

This work used an organic nanofluorophore p-FE dye, PEGylated core-shell quantum dots PbS/CdS CSQD (see Supplementary Fig. 2), ErNPs, and an organic renal excretable TT dye. p-FE is comprised of organic dyes trapped in amphiphilic polymeric micelles ~ 12 nm in size measured by dynamic light scattering[28]. The PEGylated PbS/CdS CSQD was developed recently exhibiting a wide range of excitation wavelength spanning from UV to ~ 1300 nm, high brightness, biocompatibility and liver excretion[29]. The ErNPs was based on ref. 25 and has narrow absorption spectrum around 980 nm. For a typical conjugation, 50 μL prepared PbS/CdS CSQD and 50 μL streptavidin (1 mg/mL in PBS, ProSpec) were added to 450 μL MES solution (10 mM, pH = 6.5). 60 μL EDC (65 mM in water) was freshly prepared, and added dropwise to the solution. The solution was stirred at room temperature for 3 hours. Unreacted streptavidin was removed by a centrifugal filter (cutoff = 100 k). The final product (referred to PbS/CdS-streptavidin) was suspended in 100 μL PBS buffer. 150 μg anti-mouse PD-1 (BioXCell; cat. #.: BE0146; clone RMP1–14) was dissolved in 300 μL PBS buffer. 6 μL EZ-Link™ Sulfo-NHS-LC-Biotin (1.7 mg/mL in DMSO) was added to the solution, and the solution was stirred at room temperature for 1.5 hours. Unreacted biotin was removed by a centrifugal filter (cutoff = 100 k). The final product (referred to anti-mouse- PD-1-biotin) was suspended in 100 μL PBS buffer. As prepared PbS/CdS-streptavidin and anti-mouse- PD-1-biotin was mixed, and stirred at room temperature for 2 hours. Excess antibody was removed by a centrifugal filter (cutoff = 300 k). Similar method was used to conjugate anti-mouse/human-CD11b (BioXCell; cat. #.: BE0007; clone M1/70) to PbS/CdS CSQD. The TT dye[43,49] exhibits similar spectroscopic properties as the p-FE dye with an excitation ~ 785 nm and emission ~1000–1200 nm. The TT dye contains an azide group that can be used for conjugation to PD-L1 antibodies by click chemistry for molecular imaging[50]. Purified anti-mouse-PD-L1 antibody was purchased from Selleckchem (cat. #. A2004; clone SP142). Conjugation was done through copper-free click chemistry using linker DBCO-PEG4-NHS purchased from Click Chemistry Tools[51]. Detailed information on the antibodies is included in the Life Sciences Reporting Summary.

NIR-II light sheet microscope setup

As show in Supplementary Fig. 1a, lasers with wavelengths of 658 nm, 785 nm or 1319 nm were directed into a spatial filter consisting two achromatic lenses (L3 and L4) and a 50-μm pinhole (PH), generating illumination with maximum excitation power of 1.7 mW, 11.9 mW and 8.2 mW at the front side of objective respectively. This spatial filter was introduced to improve the circularity and quality of the illumination beam and to generate uniform light sheet across the field of view. The excitations could be selected by removable mirrors (M2–

M4). Excitation power was measured by a laser power meter (3A-SH, NOVA II, OPHIR). Before the laser entering a cylindrical lens (CL), a vertically arranged adjustable mechanical slit parallel to the CL was used to adjust the span range of light sheet along Y-axis direction (Supplementary Fig. 1). A pair of achromatic lenses (L1, L2) and another slit (S1) was used for adjusting the effective numerical aperture of the objective (for adjusting light sheet shape, see below) before the light was focused on the back focal plane of illumination objective (O1) to form the light sheet illumination. For in vivo imaging, the actual excitation intensity illuminated on mouse was ~ 0.8 W cm^{-2}, ~ 1.1 W cm^{-2} and ~ 3.4 W cm^{-2} for 658 nm, 785 nm and 1319 nm laser, which is below the safety limit for laser exposure shorter than 10 s (658 nm: 1.1 W cm^{-2}; 785 nm: 1.6 W cm^{-2}, 1319 nm: 5.5 W cm^{-2})[52].

For the oblique LSM (Fig. 3e and Supplementary Fig. 1b), the optical path was the same to the normal LSM shown in Supplementary Fig. 1a but the illumination objective and the detection objective were arranged 45° to samples (Supplementary Fig. 1b). The UV fused silica right-angle prism used in oblique LSM was obtained from Thorlabs.

The light sheet was positioned to pass through a tissue sample or a tumor protrusion on a mouse or flat mouse head, fluorescence imaging was done by focusing on and normal to the light sheet plane through a detection objective (O2) and a 200-mm tube lens, using a liquid-nitrogen-cooled InGaAs camera (2D-OMA V, Princeton Instruments) or a water-cooled InGaAs camera (Ninox 640, Raptor Photonics) after filtered by selected emission filters. The focal lengths of L1, L2, L3, L4 were 60 mm, 100 mm, 30 mm and 60 mm, respectively. All the optical components were made by Thorlabs. For illumination objective, we used a 5X objective (NA = 0.15, Nikon LU Plan) or a 10X objective (NA = 0.25, Bausch & Lomb Optical Co.). For imaging, we used a 4X objective (NA = 0.1, Bausch & Lomb Optical Co.), a 10X objective (NA = 0.25, Bausch & Lomb Optical Co.) or a 50X objective (NA = 0.6, Nikon CF Plan) (see Supplementary Table 2 for combinations of objectives for various experiments).

Light sheet shape, resolution and field of view considerations

Two orthogonal slits were mounted in the illumination arm to adjust the light sheet shape by changing the effective numerical aperture NA and the span range along Y-axis direction (Supplementary Fig. 1). To observe the light sheet propagation in glycerol, water, intralipid or brain, the cylindrical lens was rotated by 90° and S1 was adjusted to control the light sheet spanning along vertical direction and S2 was used to control the actual numerical aperture (NA) of illumination. This allowed us to form light sheets with adjustable waist thickness and Raleigh length to balance imaging resolution and field of view (FOV). When 10X illumination objective and 50X detection objective were used, the effective NA of illumination was adjusted to be ~ 0.17. For 5X illumination objective and 4X or 10X detection objective, the effective NA of illumination was adjusted to be ~ 0.039 or ~ 0.051.

The effective NA was estimated using NA = $n \sin\alpha = n \sin(\arctan(D/2f))$, where n is the refractive index, α is the half of aperture angle, D is the illumination width of light sheet (adjusted by slit S1 for LSM imaging) as it exiting the illumination objective, and f is the focal length of illumination objective. At a given width of slit S1, D was measured experimentally by putting a scattering paper close to the aperture of the illumination objective. D was adjusted by S2 when the cylindrical lens was rotated by 90° for imaging the side view of the light sheet (Supplementary Fig. 7). The measured light sheet waist and Rayleigh length were consistent with those from theoretical estimations based on the effective NA values (see Supplementary Fig. 7).

The resolution of NIR-II LSM is limited by the diffraction limit and scattering that still existed in NIR-II (Fig. 1f). The diffraction limited resolution along Z for 10X, 0.25-NA detection objectives was 14.8 μm (850–1000 nm), 18.4 μm (1100–1200 nm) and 25.6 μm (1500–1700 nm) estimated by $n\lambda/\mathrm{NA}^2$.[53] The value of 25.6 μm was larger than the measured LS thickness (Supplementary Fig. 7). Therefore, resolution along Z was set by LS thickness under this condition[10], which was ~ 10 μm (Supplementary Fig. 7). Using the 0.5-NA 50X detection objective, the diffraction limited resolution along Z was 2.6 μm (850–1000 nm), 3.2 μm (1100–1200 nm), and 4.4 μm (1500–1700 nm). These analysis suggested that the Z resolution of our current NIR-II LSM is down to ~ 10 μm, suitable for single-cell resolution along Z. X-Y diffraction limited resolution was higher, ~ 2.3 μm (850–1000 nm), 2.8 μm (1100–1200 nm) and 3.9 μm (1500–1700 nm) using the 10X, 0.25-NA detection objective; and 0.9 μm (850–1000 nm), 1.2 μm (1100–1200 nm) and 1.6 μm (1500–1700 nm) using the 50X, 0.6-NA detection objective (estimated by Rayleigh criteria, $0.61\lambda/\mathrm{NA}$).

The LS waist and Rayleigh length are contradicting factors, optimizing one means degrading performance in the other. The selecting actual NA for each experiment were tradeoffs of these two parameters to obtain uniform LS that are as thin as possible across a large enough FOV. The actual NA and corresponding waist and confocal length for each data set were summarized in Supplementary Table 2.

Light sheet microscopy 3D volumetric imaging/scanning

For 3D normal NIR-II LSM imaging (Supplementary Fig. 1a), as the imaging depth changed, an obvious misalignment of light sheet and working plane of the imaging objective appeared due to refractive index mismatch of the air and tissue. This was compensated by a linear movement of detection objective (Supplementary Figs 4 and 5) concurrent with sample Z position change. The sample scanning in Z and detection objective Z compensation movement was realized by a 3D translation stage (KMTS50E, Thorlabs) and a single-axis translation stage (MTS50-Z8, Thorlabs), respectively (see Supplementary Fig. 4). Different detection windows were selected by using corresponding long-pass and short-pass filters. Synchronous control of 3D translation stage movement and image record was realized using LabView software through a data acquisition card (NI USB-6008, National Instruments).

For oblique LSM (Supplementary Fig. 1b), the lateral movement for 3D imaging was realized by a translation stage (M-VP-25XL, Newport) and another acquisition card (NI USB-6210) was used. The original images recorded by camera in oblique LSM were 45° to lateral direction (Fig. 3e). We transformed the original data to XYZ axes in ImageJ/Fiji by using the function of affine transform (shear, scaling and rotation).

Maximum intensity projections (Supplementary Fig. 12b,c) and 3D rendering was performed using ImageJ. Multi-color fluorescence images were also merged in ImageJ[54].

Mouse handling and tumor xenograft

Mouse handling was approved by Stanford University's administrative panel on Laboratory Animal Care. All experiments were performed according to the National Institutes of Health Guide for the Care and Use of Laboratory Animals. C57BL/6 and BALB/c female mice were purchased from Charles River. Bedding, nesting material, food and water were provided. 4–6-week-old C57BL/6 (or BALB/c) mice were shaved using hair removal lotion and inoculated with ~ 1 million MC38 (or CT 26) cancer cells on the right flank of back near the hindlimb or on the ear for tumor growth. The sample sizes of mice were selected based on previously reported studies. Mice were randomly selected from cages for all experiments. All relevant data are available from authors. During *in vivo* imaging, all mice were anaesthetized by a rodent anesthesia machine with 2 l min^{-1} O_2 gas mixed with 3 % isoflurane.

Ex vivo NIR-II light sheet microscopy of mouse brains

For *ex vivo* LSM of mouse brains in various NIR-I and NIR-II regions (data in Fig. 1c, Fig. 2e, Supplementary Figs 3–6 and 11), C57BL/6 mice were firstly injected with 200 μL of p-FE with O.D. = 4 at 808 nm, followed by injection of 200 μL PEGylated PbS/CdS CSQD (O.D. = 4 at 808 nm) at 5 min post injection of p-FE. The mouse was sacrificed at 30 min post injection under anesthesia, and brain tissues were taken out and fixed with 10% neutral buffered formalin at room temperature. After washing in PBS twice, the fixed mouse brain was preserved in glycerol at 4 °C for further imaging. We note that fixing and glycerol treatment induced a partial tissue clearing effect with the imaging depth increased to about twice of that in a non-cleared brain[35].

For NIR-II imaging mouse brains (data in Fig. 2a and Supplementary Fig. 12a), C57BL/6 mice were injected with 200 μL PEGylated PbS/CdS CSQD (O.D. = 4 at 808 nm) and sacrificed at 30 min post injection. The brain tissues were taken out and fixed with 10% neutral buffered formalin at room temperature. After washed in PBS twice, the fixed mouse brain was preserved in glycerol at 4 °C for *ex vivo* imaging.

For 5X illumination objective and 4X (for data in Fig. 2a) or 10X (for data in Fig. 1c, Fig. 2e, Supplementary Figs 4, 5 and 11) detection objective, the actual NA of illumination was adjusted to be ~ 0.039 or ~ 0.051. When 10X illumination objective and 50X detection objective were used, the actual NA of illumination was adjusted to be ~ 0.17 (Supplementary Fig. 6). The corresponding waists for different wavelengths were shown in Supplementary Fig. 7. Other detailed experimental conditions, such as *Z* scanning increment, exposure time, excitation and emission wavelengths, were summarized in Supplementary Table 2.

In vivo wide-field NIR-II fluorescence imaging

The NIR-II wide-field fluorescence images in Fig. 3g, Fig. 4e and Supplementary Fig. 13 were recorded using a 2D liquid-nitrogen cooled InGaAs camera (Princeton Instruments, 2D OMA-V, USA) or Ninox 640 (Raptor Photonics). An 808 nm fiber-coupled diode laser (RPMC Lasers, USA) was used as the excitation source and a filter set (850 and 1,000 nm short-pass filter) was applied to filter the excitation light. The actual excitation intensity after passing filters was ~ 70 mW cm^{-2}. The fluorescence signal was collected by two achromatic lenses to the InGaAs camera with different magnifications after filtered by corresponding low-pass and long-pass filters. Two-channel fluorescence images were merged in ImageJ.

For three-color wide-field imaging of PD-L1, PD-1 expressing cells and vessels in CT26 tumor bearing BALB/c mouse, 200 μL anti-PD-L1-Er (10 mg/mL) were injected intravenously. After 24 h, 200 μL anti-PD-1-PEGylated PbS/CdS CSQD (O.D. = 0.5 at 808 nm) were injected and in another 29 h, 250 μL p-FE (O.D. = 5 at 808 nm) was injected into the tail vein. Wide-field imaging (Fig. 3g) was performed immediately post injection of p-FE. Fluorescence signals of ErNPs (a cubic version of the NPs in ref. 25) and PbS/CdS CSQD (both in 1500–1700 nm range) were differentiated by resolving the vastly different lifetimes of the two probes (measured to be ~ 5 ms for ErNPs and ~ 20 μs for PbS). Briefly, the 1500–1700-nm fluorescence signal emitted from PbS/CdS CSQD was recorded under CW 808 nm excitation with exposure time of 5 ms, under which no fluorescence emitted from ErNPs due to the lack of absorption at 808 nm. Illumination was then switch to 975 nm pulse for 14 ms excitation. After switching off the excitation and waiting for 1 ms, wide-field imaging only detected 1500–1700-nm fluorescence from ErNPs due to its long emission lifetime (~ 5 ms, PbS CSQD ~ 20 μs) by the InGaAs camera using an exposure time of 20 ms. Finally the p-FE probes circulating in vessels were excited by a 808-nm illumination and imaged in 1100–1300 nm with an exposure time of 3 ms.

In vivo NIR-II light sheet microscopy of tumors

For three-plex light sheet imaging of PD-L1, PD-1 expressing cells and vessels in CT26 tumor on BALB/c mouse, 200 μL anti-PD-L1-Er (10 mg/mL) was first injected intravenously. After 24 h, 200 μL anti-PD-1-PEGylated PbS/CdS CSQD (O.D. = 0.5 at 808 nm) were injected. In another 29 h, 250 μL p-FE (O.D. = 5 at 808 nm) was injected into the tail vein to label the vessels. 2 min post injection of p-FE, non-invasive oblique NIR-II LSM (Fig. 3h,i,j) was performed. Two-plex PD-L1 and PD-1 were imaged by differentiating fluorescence signals of ErNPs labeled PD-L1 and PbS/CdS CSQD labeled PD-1 (both in 1500–1700 nm range) by resolving the vastly different lifetimes of the two probes (~ 5 ms for ErNP and ~ 20 μs for PbS)[25]. Briefly, the 1500–1700-nm fluorescence signal emitted from PD-1 labeled by PbS/CdS CSQD was recorded under CW 1319-nm light sheet excitation and 100-ms exposure time, during which no fluorescence emitted from ErNPs due to the lack of absorption at 1319 nm. Then illumination was switch to 14 ms long 975 nm pulse illumination and then switched off. After a wait time of 1 ms, optical sectioning/image recording of 1500–1700-nm fluorescence only detected the long life-time ErNPs for PD-L1 imaging using an exposure time of 100 ms. Fluorescence images recording at every optical sectioning was realized by synchronously controlling a 1319-nm laser, a 975-nm laser, a motorized stage and the camera using Labview software through a data acquisition card (NI USB-6210). Then another scan was performed to record p-FE signal in 1100–1300 nm in vessels with 100-ms exposure. The scanning step was 4 μm along the X direction. One step movement required 100 ms confined by the stage (M-VP-25XL, Newport).

For results shown in Supplementary Fig. 13, C57BL/6 mouse bearing a xenograft MC38 tumor on the ear or right/left flank of the back near the hindlimb was injected with anti-PD-L1-TT dye or free TT dye. The mouse was used for *in vivo* light sheet microscopy imaging immediately and at 24 hour post injection by placing the mouse on a 3D translation stage (KMTS50E, Thorlabs) after anesthesia. The initial LS illumination position *Z* below the top of the surface of the protruding tumor was controlled by the 3D motorized translation stage. For monitoring dynamic blood flow at a fixed illumination plane through the tumor (data in Fig. 3a), the camera began recording with a preset exposure time immediately after p-FE (200 μL, O.D. = 4 at 808 nm) or PEGylated PbS/CdS CSQD (200 μL, O.D. = 4 at 808 nm) was injected into the tail vein. When the recorded fluorescence images did not show further changes and reached a steady state, 3D light sheet microscopy was performed to volumetrically imaging the vasculatures or mapping the distribution of anti-PD-L1-TT in the tumor (for Supplementary Fig. 13e). For dynamic observation of blood flow (Fig. 3a, Supplementary Video 5), a 4X imaging objective lens was used. The illumination was generated by a 5X illumination objective with actual NA of ~ 0.039 (Supplementary Fig. 7). The PD-L1 were profiled using a 10X (Supplementary Fig. 13e) and a 50X (Supplementary Fig. 14b–e) detection objective. The *Z* scanning increment, exposure time and excitation and emission wavelengths were summarized in Supplementary Table 2.

In vivo NIR-II light sheet microscopy of mouse head

To image through the different layers of mouse head (Fig. 4a), 4-week-old BALB/c mouse hair were carefully shaved using hair remover lotion and washed with warm water. Then the mouse was intravenously injected with 200 μL PEGylated PbS/CdS CSQD (O.D. = 4 at 808 nm). Oblique NIR-II LSM was performed at 2 h and 12 h post injection with a 5X illumination objective and a 10X imaging objective. The mouse was mounted on a home-made stage with heating pad to keep body temperature, and imaged in the configuration shown in Supplementary Fig. 1b.

Traumatic brain injury (TBI)

The TBI was performed based on the previously reported procedures with modifications[43]. Briefly, the benchmark stereotaxic impactor was mounted on a stereotaxic frame at 45° (David Kopf Instruments, Tujunga, CA, USA). Anesthetized mice were placed on a customized foam mold in prone position. To induce TBI, the tip was driven towards mouse head at a speed of 4.0–4.5 mm/s, a dwell time of 0.2 s set by the electronic control box and an impact depth of 3 mm adjusted by the stereotaxic device. After 2 h recovery, 4–6-week-old C57BL/6 was intravenously injected with 200 μL anti-CD11b-PEGylated PbS/CdS CSQD (O.D. = 0.5 at 808 nm) and monitored by wide-field system and oblique NIR-II LSM mounted with a 5X illumination objective and a 10X imaging objective 24 h post injection. The *Z* scanning increment, exposure time and excitation and emission wavelengths were summarized in Supplementary Table 2.

Statistics and data analysis

Data analysis was performed in MATLAB 2017 or Origin 9.0. The standard deviation and mean shown in Fig.1, Fig. 2, Supplementary Fig. 4, Supplementary Fig. 6 and Supplementary Fig. 7 were calculated by Origin 9.0. The fitting lines in Supplementary Fig. 12e were derived by the weighted least-square method in Origin 9.0. For each representative experimental result, the number of successful independent experiments performed on different mice was indicated in the corresponding figure legend.

Study of light sheet propagation in different media

We experimentally compared light sheet propagation in glycerol solutions using light sheets with different NA and excitation wavelengths. These experiments were performed in glycerol containing PEGylated PbS/CdS CSQD uniformly dispersed in glycerol. The emission was collected in 1500 – 1700-nm window excited by 658-nm, 785-nm and 1319-nm LS illuminations. In order to directly observe light transmission in glycerol, we rotated the cylindrical lens by 90° and used mechanical slits to control the actual NA and the spanning range along Y (Supplementary Fig. 1a). By so doing, the illumination plane was rotated by 90° and the light sheet shape can be imaged along the Y direction for its X-Z plane for side view (Supplementary Fig. 7a). In a transparent medium (Supplementary Fig. 7a), our experimentally measured waist and double Rayleigh range of light sheet were consistent with theoretical estimations (Supplementary Fig. 7b,c).

To study the propagation of the light sheet with wavelength of 658 nm, 785 nm and 1319 nm in a scattering medium, we performed experimental imaging of LS propagation in intralipid solutions of different concentrations (Supplementary Fig. 8a). Light scattering was apparent as the intralipid concentration increased from 0.00% to 5.00 % when 658-nm or 785-nm excitation was used. Impressively, 1319-nm LS excitation retained its shape over the longest distance. We further simulated the light sheet propagation in the intralipid phantom by Monte Carlo method based on the method developed by Wang *et al.*[33] using the scattering coefficient μ_s and the anisotropy g estimated by[31,32]:

$$\mu_s(\lambda) = 0.016\lambda^{-2.4} \quad (1)$$

$$\mu_s' = 10.094 \times conc. + 0.433 \quad (2)$$

$$\mathrm{g}(\lambda) = 1.1 - 0.58\,\lambda \quad (3)$$

Where λ is the wavelength, $\mu_s' = \mu_s(1-g)$ is the reduced scattering coefficient and *conc.* is the concentration of intralipid. Equations 1 and 3 were only used for 10.00% intralipid solution[31]. The available spectral range of Equation 2 is between 750 nm to 830 nm[32]. We first calculated the μ_s of 10% intralipid solution at different wavelengths using Equations 1. Then we obtained the μ_s of 1.25%, 2.50% and 5.00% intralipid solutions based on the linear relationship between μ_s and concentration of Equation 2 and $\mu_s' = \mu_s(1-g)$. These parameters were also summarized in Supplementary Table 1.

The illumination waist measured in water at NA = 0.039 was used as initial FWHM of incident light in Monte Carlo simulations. The simulated results were consistent with the experimental observations (Supplementary Figs 8 and 9). Generally, the length over which the light sheet transmits by less than $\sqrt{2}$ times the initial waist (w_0) is regarded as the distance useful for imaging[55]. Under this definition, the critical length was larger than 1000 μm for the 1319-nm excitation in 1.25%, 2.50% and 5.00% intralipid solutions, much larger than that of 658-nm and 785-nm cases. Since the scattering coefficient of intralipid can be conveniently adjusted by controlling its concentration, it is a widely used phantom to study photon-material interactions. To study the light sheet propagation in an uniform scattering medium with similar scattering characteristics as mouse brain, we performed simulations using the scattering coefficient of the 2.5% intralipid and anisotropy factor of the brain measured by Shi *et al*[56]. We compared the simulation results with our experimental observations in glycerol-cleared mouse brain in Supplementary Fig. 10. The simulated light propagation in brain was consistent with experimental results of 658-nm, 785-nm and 1,319-nm excitation (Supplementary Fig. 10f–h). The critical distances for uniform illumination were ~ 210 μm, ~ 320 μm and ~ 1000 μm for excitations using 658 nm, 785 nm and 1319 nm light sheet in mouse brain, respectively (Supplementary Fig. 10f–h).

The LS excitation intensity along incident direction is another important parameter for imaging in scattering tissue, as it affects the transmission distance of excitation in the tissue and determines the illumination field. As the intralipid concentration increased, the intensity along propagation direction attenuated faster but the 1319-nm excitation decayed the slowest compared to the 658-nm and 785-nm excitations (Supplementary Fig. 9j–l). Intensity attenuation was influenced by scattering, absorption and anisotropy of tissue. As the brain had larger anisotropy than intralipid, light sheet transmitted longer in the brain (Supplementary Fig. 10a,b,e). In order to study the illumination field of 658-nm, 785-nm and 1319-nm LS in mouse brain, we performed LSM imaging of a brain tissue at a depth of Z ~ 200 μm along the LS incident direction X for up to 1 cm (data in Fig. 2a,b). Though photons in the LS could propagate for as far as ~ 6000 μm to excite fluorescence in large-diameter vasculatures, only in the initial limited distance that small blood vessels (FWHM < 10 μm) could be observed (Fig. 2a). These limited distances were ~1380 μm, ~1676 μm and ~3900 μm for 658-nm, 785-nm and 1319-nm excitation respectively as longer excitation attenuated slower in mouse brain.

For high-quality optical sectioning in LSM, both uniform light sheet waist and available illumination field need to be ensured across the field of view.

Data availability

The data that support the findings of this study are available from the corresponding author upon request.

Supplementary Material

Refer to Web version on PubMed Central for supplementary material.

Acknowledgments

We thank members of the Dai group for discussion. This study was supported by the National Institutes of Health NIH DP1-NS-105737.

References

1. Jain RK Antiangiogenesis strategies revisited: From starving tumors to alleviating hypoxia. Cancer Cell 26, 605–622 (2014). [PubMed: 25517747]
2. Liu T-L, Upadhyayula S, Milkie DE et al. Observing the cell in its native state: Imaging subcellular dynamics in multicellular organisms. Science 360, eaaq1392 (2018). [PubMed: 29674564]
3. Helmchen F & Denk W Deep tissue two-photon microscopy. Nat. Methods 2, 932–940 (2005). [PubMed: 16299478]
4. Lapadula G, Bourdolle A, Allouche F et al. Near-IR two photon microscopy imaging of silica nanoparticles functionalized with isolated sensitized Yb(III) centers. Chem. Mater 26, 1062–1073 (2014).
5. Alifu N, Yan LL, Zhang HQ et al. Organic dye doped nanoparticles with NIR emission and biocompatibility for ultra-deep in vivo two-photon microscopy under 1040 nm femtosecond excitation. Dyes Pigments 143, 76–85 (2017).
6. Horton NG, Wang K, Kobat D et al. In vivo three-photon microscopy of subcortical structures within an intact mouse brain. Nat. Photonics 7, 205–209 (2013).
7. Ouzounov DG, Wang TY, Wang MR et al. In vivo three-photon imaging of activity of GCaMP6-labeled neurons deep in intact mouse brain. Nat. Methods 14, 388–390 (2017). [PubMed: 28218900]
8. Rowlands CJ, Park D, Bruns OT et al. Wide-field three-photon excitation in biological samples. Light-Sci. Appl 6, e16255 (2017). [PubMed: 29152380]
9. Liu J, Wu R, Li N et al. Deep, high contrast microscopic cell imaging using three-photon luminescence of β-(NaYF4:Er3+/NaYF4) nanoprobe excited by 1480-nm CW laser of only 1.5-mW. Biomed. Opt. Express 6, 1857–1866 (2015). [PubMed: 26137385]
10. Huisken J, Swoger J, Del Bene F, Wittbrodt J & Stelzer EHK Optical sectioning deep inside live embryos by selective plane illumination microscopy. Science 305, 1007–1009 (2004). [PubMed: 15310904]
11. Dodt HU, Leischner U, Schierloh A et al. Ultramicroscopy: three-dimensional visualization of neuronal networks in the whole mouse brain. Nat. Methods 4, 331–336 (2007). [PubMed: 17384643]
12. Truong TV, Supatto W, Koos DS, Choi JM & Fraser SE Deep and fast live imaging with two-photon scanned light-sheet microscopy. Nat. Methods 8, 757–U102 (2011). [PubMed: 21765409]
13. Escobet-Montalbán A, Gasparoli FM, Nylk J et al. Three-photon light-sheet fluorescence microscopy. Opt. Lett 43, 5484–5487 (2018). [PubMed: 30383037]
14. Chung K, Wallace J, Kim S-Y et al. Structural and molecular interrogation of intact biological systems. Nature 497, 332–337 (2013). [PubMed: 23575631]
15. Tomer R, Ye L, Hsueh B & Deisseroth K Advanced CLARITY for rapid and high-resolution imaging of intact tissues. Nat. Protoc 9, 1682–1697 (2014). [PubMed: 24945384]
16. Bouchard MB, Voleti V, Mendes CS et al. Swept confocally-aligned planar excitation (SCAPE) microscopy for high-speed volumetric imaging of behaving organisms. Nat. Photonics 9, 113 (2015). [PubMed: 25663846]
17. Welsher K, Liu Z, Sherlock SP et al. A route to brightly fluorescent carbon nanotubes for near-infrared imaging in mice. Nat. Nanotechnol 4, 773–780 (2009). [PubMed: 19893526]
18. Welsher K, Sherlock SP & Dai HJ Deep-tissue anatomical imaging of mice using carbon nanotube fluorophores in the second near-infrared window. P. Natl. Acad. Sci. USA 108, 8943–8948 (2011).
19. Hong G, Lee JC, Robinson JT et al. Multifunctional in vivo vascular imaging using near-infrared II fluorescence. Nat. Med 18, 1841–1846 (2012). [PubMed: 23160236]
20. Hong GS, Diao S, Chang JL et al. Through-skull fluorescence imaging of the brain in a new near-infrared window. Nat. Photonics 8, 723–730 (2014). [PubMed: 27642366]
21. Hong GS, Zou YP, Antaris AL et al. Ultrafast fluorescence imaging in vivo with conjugated polymer fluorophores in the second near-infrared window. Nat. Commun 5, 4206 (2014). [PubMed: 24947309]

22. Diao S, Blackburn JL, Hong GS et al. Fluorescence imaging in vivo at wavelengths beyond 1500 nm. Angew. Chem. Int. Edit 54, 14758–14762 (2015).
23. Diao S, Hong GS, Antaris AL et al. Biological imaging without autofluorescence in the second near-infrared region. Nano Res. 8, 3027–3034 (2015).
24. Antaris AL, Chen H, Cheng K et al. A small-molecule dye for NIR-II imaging. Nat. Mater 15, 235–242 (2016). [PubMed: 26595119]
25. Zhong YT, Ma ZR, Zhu SJ et al. Boosting the down-shifting luminescence of rare-earth nanocrystals for biological imaging beyond 1500 nm. Nat. Commun 8, 737 (2017). [PubMed: 28963467]
26. Won N, Jeong S, Kim K et al. Imaging depths of near-infrared quantum dots in first and second optical windows. Mol. Imaging 11, 338–352 (2012). [PubMed: 22954148]
27. Naczynski DJ, Tan MC, Zevon M et al. Rare-earth-doped biological composites as in vivo shortwave infrared reporters. Nat. Commun 4, 2199 (2013). [PubMed: 23873342]
28. Wan H, Yue J, Zhu S et al. A bright organic NIR-II nanofluorophore for three-dimensional imaging into biological tissues. Nat. Commun 9, 1171 (2018). [PubMed: 29563581]
29. Zhang M, Yue J, Cui R et al. A Bright Fluorescent Probe Emitting at ~ 1600 nm for in Vivo fluorescence imaging. P. Natl. Acad. Sci. USA 115, 6590–6595 (2018).
30. Bruns OT, Bischof TS, Harris DK et al. Next-generation in vivo optical imaging with short-wave infrared quantum dots. Nat. Biomed. Eng 1, 0056 (2017). [PubMed: 29119058]
31. van Staveren HJ, Moes CJM, van Marie J, Prahl SA & van Gemert MJC Light scattering in lntralipid-10% in the wavelength range of 400–1100 nm. Appl. Opt 30, 4507–4514 (1991). [PubMed: 20717241]
32. Johns M, Giller CA, German DC & Liu HL Determination of reduced scattering coefficient of biological tissue from a needle-like probe. Opt. Express 13, 4828–4842 (2005). [PubMed: 19498468]
33. Wang L, Jacques SL & Zheng L MCML—Monte Carlo modeling of light transport in multi-layered tissues. Comput. Meth. Prog. Bio 47, 131–146 (1995).
34. Shi L & Alfano RR Deep imaging in tissue and biomedical materials: using linear and nonlinear optical methods. (CRC Press, 2017).
35. Song E, Ahn Y, Ahn J et al. Optical clearing assisted confocal microscopy of ex vivo transgenic mouse skin. Opt Laser Technol 73, 69–76 (2015).
36. Maeda A, Leung MKK, Conroy L et al. In vivo optical imaging of tumor and microvascular response to ionizing radiation. Plos One 7, e42133 (2012). [PubMed: 22927920]
37. Balar AV & Weber JS PD-1 and PD-L1 antibodies in cancer: current status and future directions. Cancer Immunol. Immun 66, 551–564 (2017).
38. Song M, Chen D, Lu B et al. PTEN Loss Increases PD-L1 Protein Expression and Affects the Correlation between PD-L1 Expression and Clinical Parameters in Colorectal Cancer. Plos One 8, e65821 (2013). [PubMed: 23785454]
39. Tang HD, Wang Y, Chlewicki LK et al. Facilitating T Cell Infiltration in Tumor Microenvironment Overcomes Resistance to PD-L1 Blockade. Cancer Cell 29, 285–296 (2016). [PubMed: 26977880]
40. Wang TY, Ouzounov DG, Wu CY et al. Three-photon imaging of mouse brain structure and function through the intact skull. Nat. Methods 15, 789–792 (2018). [PubMed: 30202059]
41. Kawakami R, Sawada K, Kusama Y et al. In vivo two-photon imaging of mouse hippocampal neurons in dentate gyrus using a light source based on a high-peak power gain-switched laser diode. Biomed. Opt. Express 6, 891–901 (2015). [PubMed: 25798313]
42. Herisson F, Frodermann V, Courties G et al. Direct vascular channels connect skull bone marrow and the brain surface enabling myeloid cell migration. Nat. Neurosci 21, 1209–1217 (2018). [PubMed: 30150661]
43. Zhang XD, Wang HS, Antaris AL et al. Traumatic Brain Injury Imaging in the Second Near-Infrared Window with a Molecular Fluorophore. Adv. Mater 28, 6872–6879 (2016). [PubMed: 27253071]
44. Russo MV & McGavern DB Inflammatory neuroprotection following traumatic brain injury. Science 353, 783–785 (2016). [PubMed: 27540166]

45. Itoh R, Landry JR, Hamann SS & Solgaard O Light sheet fluorescence microscopy using high-speed structured and pivoting illumination. Opt. Lett 41, 5015–5018 (2016). [PubMed: 27805674]
46. Tomer R, Lovett-Barron M, Kauvar I et al. SPED light sheet microscopy: Fast mapping of biological system structure and function. Cell 163, 1796–1806 (2015). [PubMed: 26687363]
47. Pediredla AK, Zhang SZ, Avants B et al. Deep imaging in scattering media with selective plane illumination microscopy. J Biomed Opt 21, 126009 (2016). [PubMed: 27997019]
48. Keller PJ, Schmidt AD, Santella A et al. Fast, high-contrast imaging of animal development with scanned light sheet-based structured-illumination microscopy. Nat. Methods 7, 637–U655 (2010). [PubMed: 20601950]
49. Weizhi W, Zhuoran M, Shoujun Z et al. Molecular Cancer Imaging in the Second Near-Infrared Window Using a Renal-Excreted NIR-II Fluorophore-Peptide Probe. Adv. Mater 0, 1800106 (2018).
50. Wan H, Ma H, Zhu S et al. Developing a Bright NIR-II Fluorophore with Fast Renal Excretion and Its Application in Molecular Imaging of Immune Checkpoint PD-L1. Advanced Functional Materials 28, 1804956 (2018).
51. Zhu SJ, Yang QL, Antaris AL et al. Molecular imaging of biological systems with a clickable dye in the broad 800-to 1,700-nm near-infrared window. P. Natl. Acad. Sci. USA 114, 962–967 (2017).
52. Matthes R, Cain CP, Courant D et al. Revision of guidelines on limits of exposure to laser radiation of wavelengths between 400 nm and 1.4 mu m. Health Phys 79, 431–440 (2000). [PubMed: 11007467]
53. Hell SW Far-field optical nanoscopy. Science 316, 1153–1158 (2007). [PubMed: 17525330]
54. Schindelin J, Arganda-Carreras I, Frise E et al. Fiji: an open-source platform for biological-image analysis. Nat. Methods 9, 676–682 (2012). [PubMed: 22743772]
55. Power RM & Huisken J A guide to light-sheet fluorescence microscopy for multiscale imaging. Nat. Methods 14, 360–373 (2017). [PubMed: 28362435]
56. Shi LY, Sordillo LA, Rodriguez-Contreras A & Alfano R Transmission in near-infrared optical windows for deep brain imaging. J. Biophotonics 9, 38–43 (2016). [PubMed: 26556561]

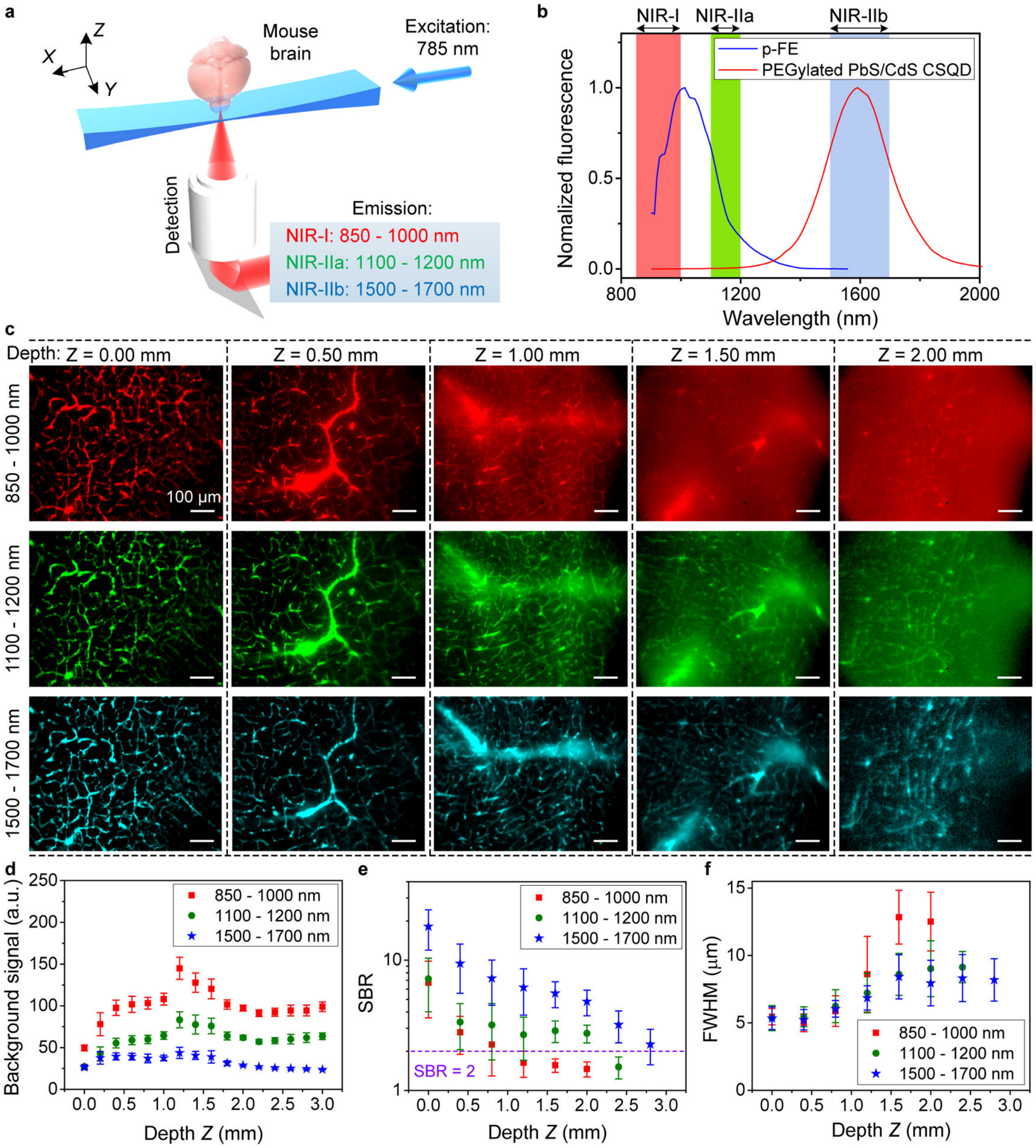

Figure 1 |. Light sheet microscopy in various NIR 850–1700 nm emission sub-regions in glycerol-cleared brain tissues.

(**a**) A simplified schematic of the NIR-II LSM. (**b**) Fluorescence emission spectra of p-FE and PEGylated PbS/CdS core/shell quantum dots (see Supplementary Fig. 2 for excitation spectra). Similar results for *n* = 5 independent experiments. (**c**) Light-sheet optical sectioning mouse brain vasculatures at various depths in NIR-I, NIR-IIa and NIR-IIb emission regions using the same 785 nm light sheet illumination kept constant power (0.33 mW) at different depths (also see Supplementary Video 1). Similar results for *n* = 3 (C57BL/6, female, 6 weeks old). The color bar range for each image is shown in Supplementary Fig. 3. Comparison of (**d**) background signal, (**e**) signal-to-background ratio (SBR) and (**f**) FWHM of smallest vessels at various depths. Background was measured from randomly selected area without vasculatures. SBR is the ratio of fluorescence signals in randomly selected vasculatures over the background. (**d**-**f**) The centre values are mean and error bars representing standard deviation were derived from analyzing ~ 10 target data at every depth. A 10X (NA = 0.25) imaging objective and a 5X illumination objective (effective NA = 0.039, light sheet waist $w = \sim 15.2$ µm and Rayleigh length $b = \sim 1258.2$ µm for 785-nm excitation, see Methods for light sheet shape analysis) were used in these experiments. Scale bars are 100 µm for all images in (**c**).

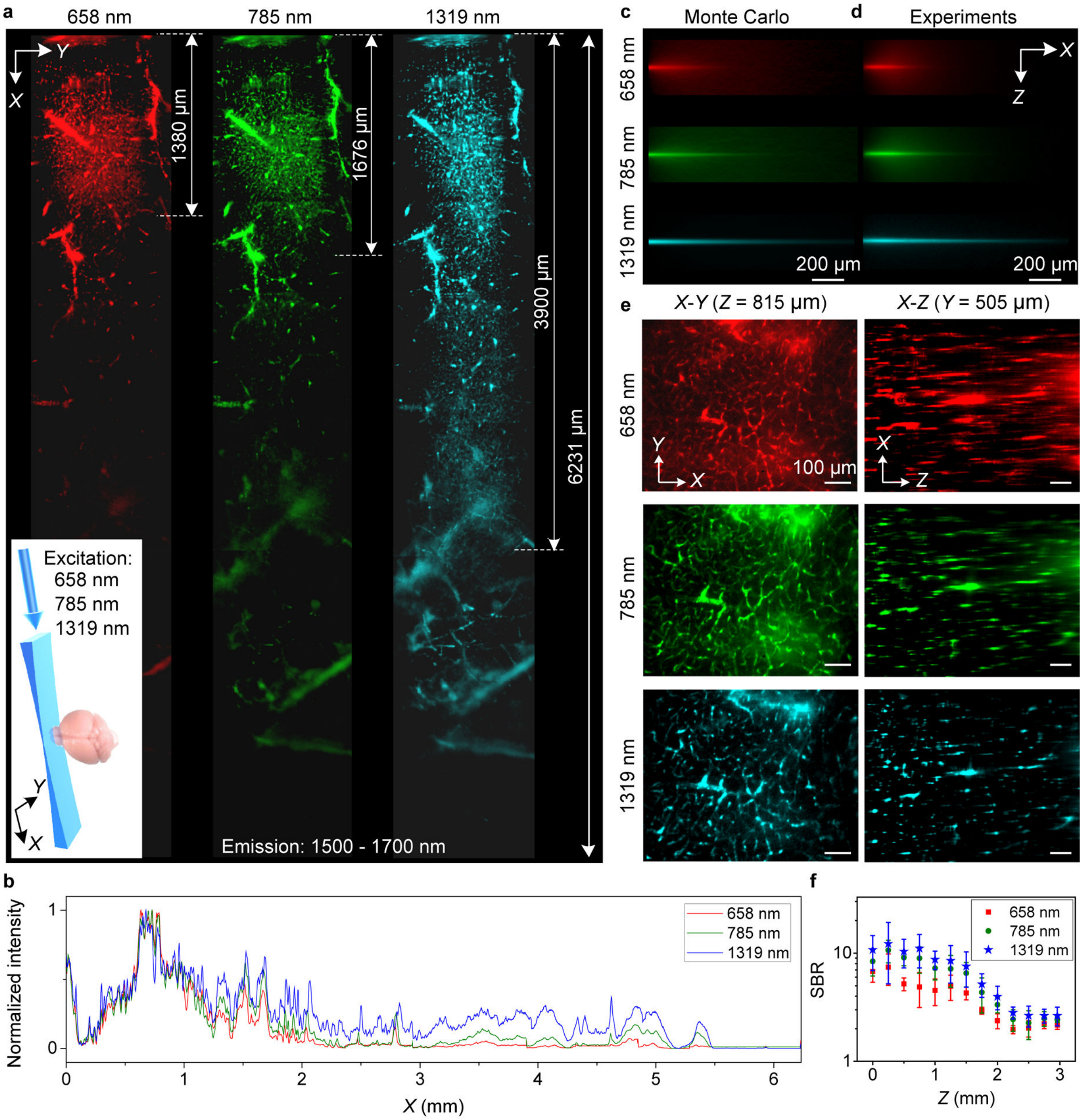

Figure 2 |. Propagation of light sheet excitation with progressively longer wavelength up to 1319 nm in glycerol-cleared brain tissues.

(**a**) *X*-*Y* images of 1500–1700 nm quantum dot fluorescence in the vasculatures of a fixed brain tissue at a depth *Z* = ~ 200 μm under 658 nm (0.22 mW), 785 nm (0.33 mW) and 1319 nm (1.4 mW) light sheet illumination as shown in the inset. 6 images were taken along *X* and stitched together for each light sheet. (**b**) Normalized sum intensity along *Y* direction of images in (**a**) as a function of propagation distance (*X*). Similar results for *n* = 2 (C57BL/6, female, 6 weeks old). (**c**) Monte Carlo simulations and (**d**) experimental results showing the *X*-*Z* propagations of different wavelengths light sheets in 2.5% intralipid tissue phantom (mimicking the brain) containing PEGylated PbS/CdS CSQD. Similar results for *n* = 3 independent experiments. Scattering coefficients were summarized in Supplementary Table 1. (**e**) Left: *X*-*Y* images of quantum dot 1500–1700 nm fluorescence in brain vasculatures taken at Z = 925 m under excitations by 658 nm, 785 nm and 1319 nm light sheets respectively (Supplementary Video 2). Right: images along the X-Z plane at a fixed Y, reconstructed from X-Y images at various depth Z (Supplementary Video 3). A 10X, 0.25-NA detection objective was used and LS excitation was generated by a 5X illumination objective with an effective NA of ~ 0.039. Similar results for n = 3 (C57BL/6, female, 6 weeks old). (**f**) Comparison of SBR for X-Y images recorded at different depth for 658 nm, 785 nm and 1319 nm excitation. About 10 randomly selected vasculatures and 10 areas without vasculatures were analyzed to calculate SBR at each depth. The centre values are mean and error bars represent standard deviation. Scale bars, 200 μm (**c**,**d**) and 100 μm (**e**).

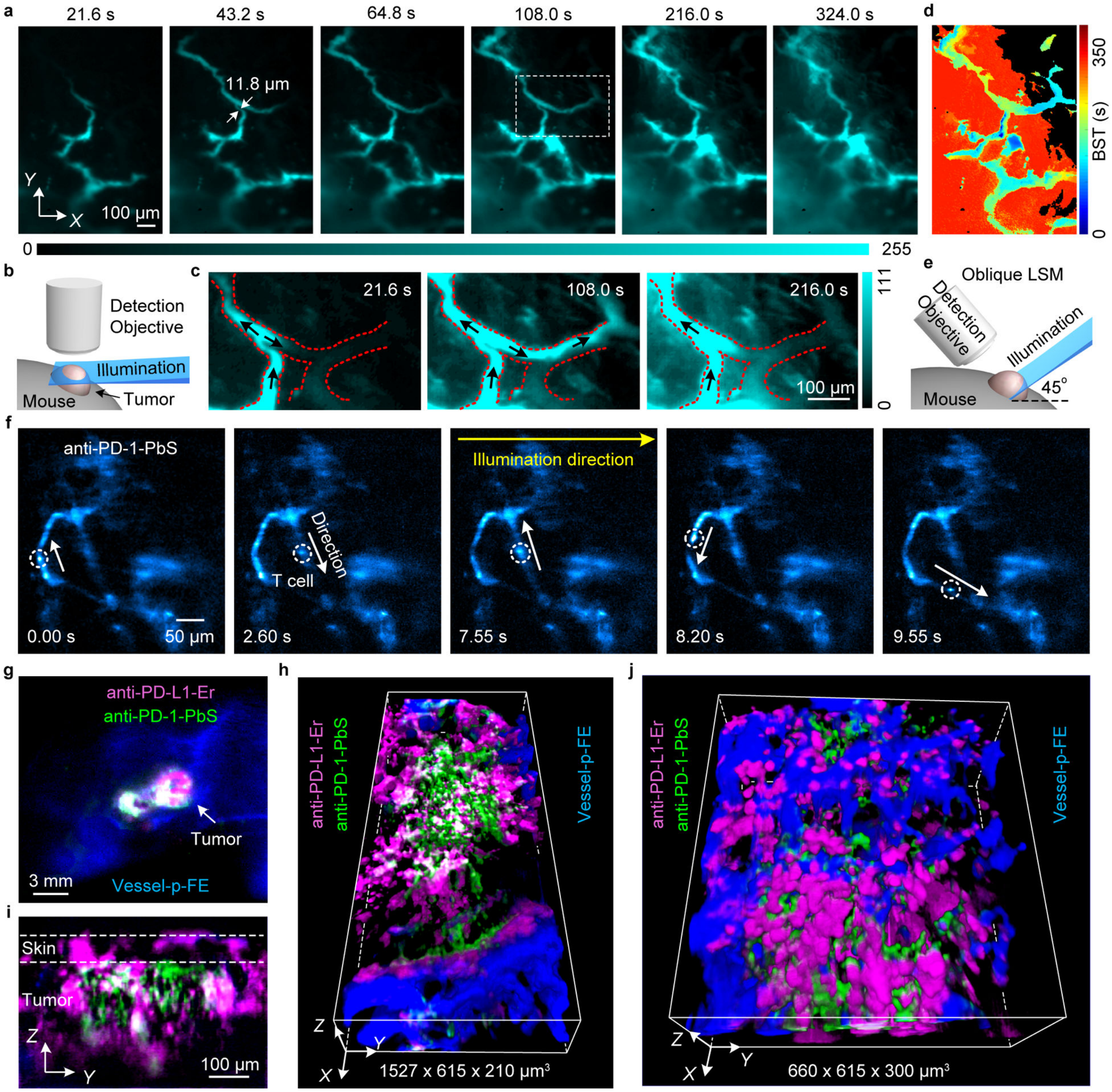

Figure 3 |. Non-invasive *in vivo* NIR-II light sheet microscopy of tumors on mice.

(**a**) Time-course (Supplementary Video 5) LSM of tumor vasculatures at a fixed illumination plane below the top of a xenograft MC38 tumor on mouse ear at *Z* ~ 300 μm after intravenous injection of p-FE (excitation: 785 nm, emission: 1000–1200 nm). A 4X detection objective and a 5X illumination objective in a normal, non-oblique configuration of (**b**) were used. (**c**) Abnormal blood flows in tumor vessels, showing on-off intermittency and direction reversal in the rectangular highlighted region in (**a**) and gradual extravasation into tumor space (Supplementary Video 5). Similar results for *n* = 3 (C57BL/6, female, 6 weeks old). Black arrows represent flow direction. (**d**) A BST map showing highly heterogeneous blood perfusion in tumor vessels and slow, inhomogeneous extravasation behavior into tumor space (C57BL/6, female, 6 weeks old; similar results for *n* = 2). (**e**)

Schematic illustration of *in vivo* oblique NIR-II LSM with illumination and detection at 45° to mouse body (Supplementary Fig.1b). (**f**) Time-course (Supplementary Video 6) recording of PD-1+ cells (white circles) in a CT26 tumor labeled by anti-PD-1-CSQDs 2 h after intravenous injection of anti-PD-1-CSQDs at 20 fps by oblique LSM (Supplementary Video 6). (**g**) Wide-field imaging of anti-PD-L1-Er (magenta), anti-PD-1-PEGylated PbS/CdS CSQD (green) labeled cells and p-FE filling vessels (blue) in a CT26 tumor. (**h)** Non-invasive *in vivo* three-plex 3D light sheet microscopy of anti-PD-L1-Er, anti-PD-1-PEGylated PbS/CdS CSQD and vasculatures (p-FE), which is ~ 120 μm beneath the surface in a CT26 tumor. (**i**) A *Y-Z* cross section of tumor in (**g**). (**j**) A local zoom three-plex 3D LSM of the tumor in (**g**) (Supplementary Video 7). (**f-j**) Similar results for $n = 2$ (BALB/c, female, 6 weeks old). (**a**,**c**) were imaged by NIR-II LSM shown in (**b**). (**f**,**h-j**) were obtained using oblique NIR-II LSM (**e**).

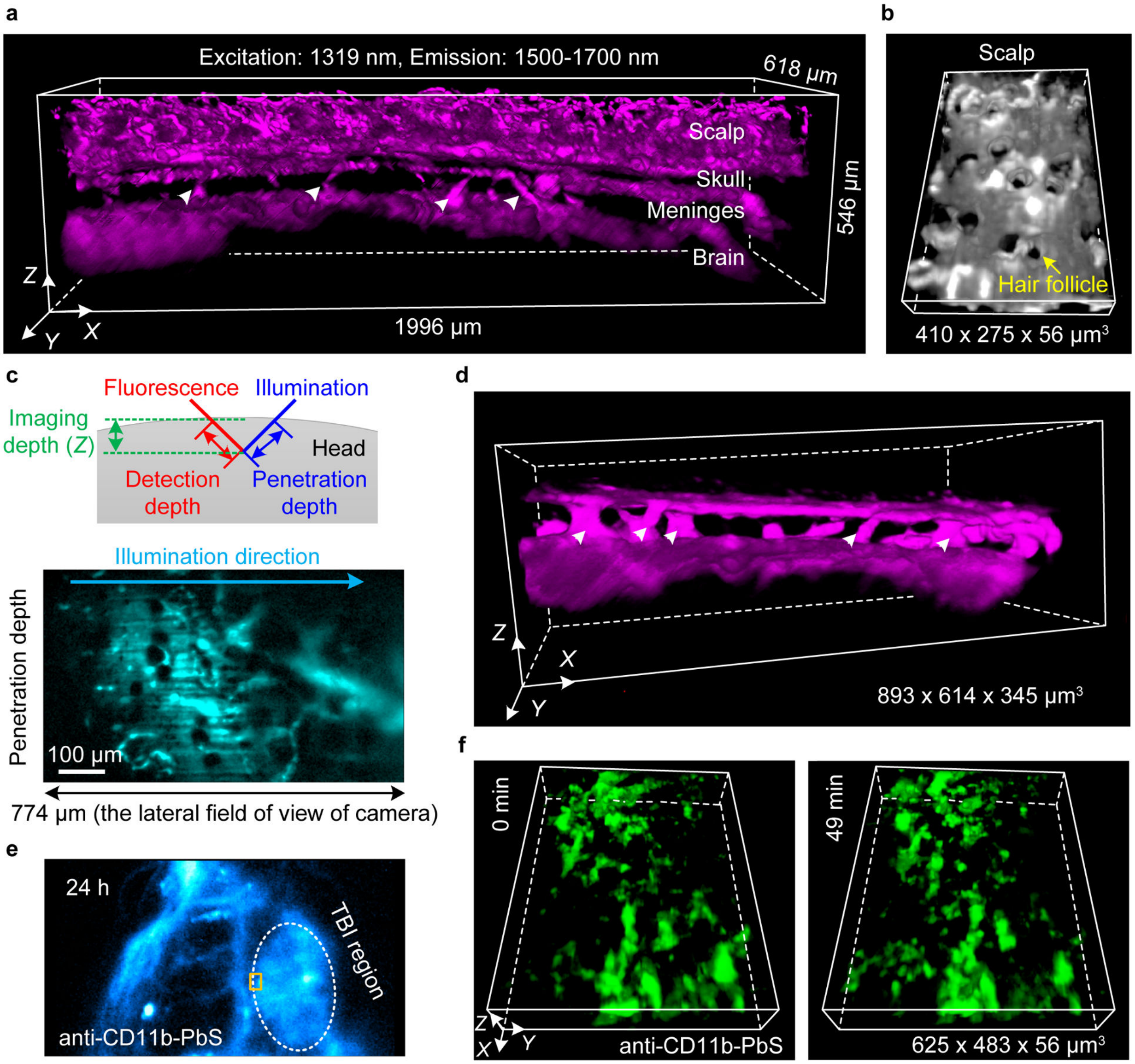

Figure 4 |. Non-invasive *in vivo* light sheet imaging of mouse head by oblique NIR-II LSM.

(**a**) A 3D reconstructed image of blood vessels in an intact mouse through the scalp, skull, meninges and brain cortex obtained 2 h after intravenous injection of PEGylated PbS/CdS CSQD by an oblique NIR-II LSM shown in Fig. 3e. The white triangles point to the vascular channels connecting the brain cortex and skull in the meninges. (**b**) A zoomed-in 3D view of the scalp layer showing follicle structures. (**c**) Top: a schematic diagram showing the definitions of penetration depth, detection depth and imaging depth in oblique NIR-II LSM. The illumination direction was ~ 45° to mouse head. Bottom: an original image recording a cross section along the illumination direction in (**a**) crossing the full field of field (FOV) of camera when a 10X imaging objective was used. (**a-c**) Similar imaging were performed at 3 positions of mouse head in each of 2 mice (BALB/c, female, 4 weeks old), for a total *n* = 6. (**d**) A 3D reconstructed image of vascular channels (triangles marks) in the meninges obtained at a later time point 12 h after injection of PEGylated PbS/CdS CSQD with 4-μm scan increment along X axis and 10-ms exposure (BALB/c, female, 4 weeks old; similar results for $n = 2$). (**e**) Wide-field traumatic brain injury (TBI) imaging of mouse head 26 h after injury and 24 h after intravenous injection of anti-CD11b-PEGylated PbS/CdS CSQD. (**f**) 3D time-course light sheet imaging/monitoring of meningeal macrophages/ microglia dynamics following brain injury 24 h after injection of anti-CD11b-PEGylated PbS/CdS CSQD at the boundary of TBI region (rectangular marked area in (**e**)). CD11b+ macrophages/ microglia labeled recruited to the injury was monitored (BALB/c, female, 4 weeks old; similar results for $n = 2$; Supplementary Video 8).